

Research papers

Modulation of hierarchical porosity in metal-doping graphene/carbon hybrid aerogels for capacitive energy storage

Guojie Chao^a, Dong Wang^b, Yang Wang^a, Xu Zhang^a, Suli Chen^a, Yufeng Wang^b, Wei Zong^b, Wei Fan^b, Longsheng Zhang^{a,*}, Tianxi Liu^{a,*}

^a Key Laboratory of Synthetic and Biological Colloids, Ministry of Education, School of Chemical and Material Engineering, International Joint Research Laboratory for Nano Energy Composites, Jiangnan University, Wuxi, China

^b State Key Laboratory for Modification of Chemical Fibers and Polymer Materials, College of Materials Science and Engineering, Donghua University, Shanghai, China



ARTICLE INFO

Keywords:

Supercapacitor
Electrode material
Carbon aerogel
Hierarchical porosity

ABSTRACT

Carbon aerogels hold great promise as the electrode materials for energy storage owing to their desirable porous structures and specific surface areas. Here, we report a scalable approach for the preparation of Co-doped graphene/carbon hybrid aerogel (CGCA) with hierarchically porous structure through a dual cross-linking strategy. By adjusting the cross-linking structure of the hydrogel precursor, the porous structure of CGCA can be readily regulated and the specific surface area of CGCA can achieve $1217 \text{ m}^2 \text{ g}^{-1}$. As a result, the CGCA samples not only manifest improved electrical conductivity, but also possess enhanced capacitance storage capacity. The optimized CGCA electrode displays a high specific capacitance of 371 F g^{-1} at 1 A g^{-1} and maintains a large specific capacitance of 57 % at 150 A g^{-1} . Meanwhile, the supercapacitor assembled with CGCA electrodes shows a high specific capacitance of 80 F g^{-1} at 0.5 A g^{-1} and good cyclic stability with a capacitance retention of 95 % after 10,000 cycles. Moreover, the supercapacitor device can provide a high energy density of 11.1 Wh kg^{-1} at a power density of 250 W kg^{-1} . The superior energy-storage behaviors of CGCA make them promising electrode materials for high-performance supercapacitors.

1. Introduction

The ever-growing global energy demands and environmental issues nowadays have accelerated the development of renewable energy. As the highly promising energy-storage systems, the supercapacitors receive a lot of attention because of their high-power density, long cycle life, environment-friendly property and wide operating-temperature range [1–6]. Accordingly, great efforts have been made to prepare high performance and low-cost electrode materials to realize the large-scale application of supercapacitors. To date, carbon materials have shown their potentials as low-cost and highly-durable electrode materials for supercapacitors, whose capacitive energies are stored by electric double-layer capacitor (EDLC) between electrolytes and electrode materials [7–9]. However, the carbon materials usually have poor EDLC ($<100 \text{ F g}^{-1}$) [10], which seriously affects the capacitive performance of the supercapacitors with carbon-based electrode materials. According to the literatures [11–13], the capacitive performance of carbon materials can be effectively promoted through the pore engineering. Therefore,

the researchers are currently devoted to modulate the porous structures of carbon-based electrode materials and increase their specific surface areas to boost their EDLC-derived capacitive properties.

With the attractive features of large specific surface area and superior mass-transfer capability, the three-dimensional (3D) porous carbon aerogels (CA) have been extensively investigated as the inspiring electrode materials for supercapacitors [14–18]. Unfortunately, as for the low bulk density and high surface area, the CA materials usually show poor electrical conductivity, resulting in reduced charge transfer and power density [19]. While, the high conductivity of CA materials can be achieved through graphitization to build better-connected structures, but this method usually reduces the surface area and porosity of these prepared CA materials [20]. Therefore, it is a challenge to combine the high surface area and high conductivity of CA materials.

Recently, lots of efforts have been done in the design and preparation of carbon-based composite aerogels to implement the desired combination of properties and synergies through multiple components [21–24]. As reported, the carbon materials can be combined with

* Corresponding authors.

E-mail addresses: zhangls@jiangnan.edu.cn (L. Zhang), txliu@jiangnan.edu.cn (T. Liu).

<https://doi.org/10.1016/j.est.2022.105445>

Received 15 June 2022; Received in revised form 20 July 2022; Accepted 6 August 2022
2352-152X/© 2022 Elsevier Ltd. All rights reserved.

polymers to prepare prefabricated polymer hydrogels, which can be converted to carbon aerogels through subsequent freeze-drying and carbonization processes [25–28]. Among others, the graphene oxide (GO) sheets work well as the cross-linking agents to anchor polymer chains to prepare the carbon-based composite aerogels with improved mechanical property and enhanced electrochemical advantages [29–33]. Meanwhile, it is an effective way to modulate the hierarchical porosity of carbon aerogels by adjusting the cross-linking points of the prefabricated polymer hydrogels [34–37]. According to the literatures, the metal ions are effective cross-linking points to anchor polymer chains to form metal-polymer gel precursors for the preparation of porous CA materials [38–40], which is conducive to obtaining porous materials with high conductivity. On these bases, we propose that the prefabricated composite hydrogels can be synthesized using GO sheets and metal ions as the dual cross-linking agents, which is expected to prepare CA materials with high conductivity and high specific surface area, achieving high capacitive performance of CA materials.

Here, we reported a well-designed Co-doped graphene/carbon hybrid aerogel (CGCA) using a dual cross-linking strategy derived from cobalt ions (Co^{2+}) and GO cross-linked polyamic acid (PAA) hydrogel. The PAA was employed as the skeleton material to construct the three-dimensional structure of the aerogels, which could provide good mechanical properties to maintain the porous structure through imidization. Meanwhile, with Co^{2+} and GO sheets as dual cross-linking agents, the molecular chains of PAA were effectively anchored and the pore structure of CGCA could be adjusted by tuning the crosslinking degree of hydrogel precursor. Due to the multi-porous architecture, the specific surface area of CGCA can even achieve $1217 \text{ m}^2 \text{ g}^{-1}$ with pores ranging from micropore to mesopore. In addition, the graphitization degree of CGCA can be enhanced because of the Co doping and the presence of N and O elements can promote the wettability of the CGCA, thus improving the conductivity and making the electrolyte easily penetrate into the porous electrode material. With the advantages of hierarchically porous structures and multielement doping, the CGCA has a high specific capacitance of 371 F g^{-1} at 1 A g^{-1} , which can remain about 57 % of the initial capacitance at 150 A g^{-1} . Moreover, the supercapacitor with CGCA-2 electrodes provides a large high energy density of 11.1 Wh kg^{-1} at a power density of 250 W kg^{-1} . This work provides a facile and scalable approach for the preparation of carbon-based hybrid aerogel with high electrical conductivity and hierarchically porous structure to achieve the enhanced capacitive energy storage.

2. Experimental section

2.1. Preparation of CGCA

Firstly, the PAA was synthesized according to the previous reports [41,42], and the specific experimental steps were shown in Supplementary material. Then, the PAA (1 g) and triethanolamine (1 g) were immersed into 10 ml GO solution (8 mg mL^{-1}) under stirring. When PAA was completely dissolved, the $\text{CoCl}_2 \cdot 6\text{H}_2\text{O}$ solution was added under stirring. At rest for 24 h, the solution went from a liquid state to a gel state, which resulted in the Co^{2+} and GO cross-linked PAA hydrogel (CGPH). By regulating the amount of $\text{CoCl}_2 \cdot 6\text{H}_2\text{O}$, a series of CGPH samples were prepared, which were named as CGPH-1 (0.2 g $\text{CoCl}_2 \cdot 6\text{H}_2\text{O}$), CGPH-2 (0.4 g $\text{CoCl}_2 \cdot 6\text{H}_2\text{O}$) and CGPH-3 (0.6 g $\text{CoCl}_2 \cdot 6\text{H}_2\text{O}$), respectively. For comparison, the PAA-based hydrogel (PH) and the GO cross-linking PAA hydrogel (GPH) were also prepared. After freeze-drying for 2 days, the dried gel samples could be obtained. Then, the dried gel samples were imidized at $350 \text{ }^\circ\text{C}$ for 1 h and carbonized at $800 \text{ }^\circ\text{C}$ for 2 h in a tubular furnace in Ar. Finally, the obtained carbon aerogels were named as PCA (PH-derived), GCA (GPH-derived), CGCA-1 (CGPH-1-derived), CGCA-2 (CGPH-2-derived) and CGCA-3 (CGPH-3-derived), respectively.

2.2. Preparation of electrode

The slurry-coating approach was employed to prepare the working electrodes and the carbon papers were used as the current collectors during the electrochemical tests. Using the slurry-coating approach, the amount of electrode materials can be readily adjusted by controlling the amount of electrode slurries used to paste on the current collectors. The acetylene black, polyvinylidene fluoride, *N*-methyl-2-pyrrolidone (NMP) were employed as conductive agent, binder and solvent, respectively. Under tiring, the prepared CA materials, binder and conductive agent were mixed into NMP in a weight ratio of 8:1:1 to prepare the ink. Then, the electrodes were prepared by homogeneous coating the ink (1 mg) on carbon paper ($1 \times 1 \text{ cm}^2$) and dried overnight at $80 \text{ }^\circ\text{C}$. The electrochemical tests were carried in $1 \text{ M H}_2\text{SO}_4$ electrolyte or 6 M KOH electrolyte. The detailed electrochemical testing process and related calculation were shown in the Supplementary materials.

3. Result and discussion

3.1. Preparation of CGCA materials

As illustrated in Fig. 1, the CGCA was schematically obtained by a simple two-step method. Firstly, a series of PAA-based hydrogels were synthesized by controlling the type and amount of cross-linking agent (Fig. 2a). For the Co^{2+} and GO cross-linked PAA hydrogel (CGPH), the Co^{2+} and the GO sheets could link the oxygen-containing groups and amide groups of PAA chains as the dual cross-linking points. Moreover, the Co^{2+} could connect the oxygen-containing groups of GO sheets and PAA chains via coordinate interactions. In addition, the physical cross-linking points were established due to the entangled PAA molecular chains. Simultaneously, the H-bond between the oxygen-containing groups of GO sheets and the amide groups of PAA chains could also improve the mechanical performance of CGPH. These physical and chemical cross-linking points were able to structure the 3D cross-linking networks of CGPH with good mechanical properties. As shown in stress-strain curves of these obtained hydrogels (Fig. 2b), it is clear that the tensile stress of the GO sheets cross-linked PAA hydrogel (GPH) is higher than that of the PAA hydrogel without cross-linker (PH), but much lower than those of CGPH samples with dual cross-linking points, illustrating that the dual cross-linking strategy can effectively promote the mechanical performance of the prefabricated PAA-based hydrogels. Moreover, the CGPH-2 manifests the highest tensile stress and the strongest modulus among these samples, illustrating that the CGPH-2 has the outstanding cross-linking strength. The above results may be attributed to the moderate amount of cross-linking points and good cross-linking state of CGPH-2. The insufficient Co^{2+} content leads to insufficient cross-linking degree of hydrogels, while the high amount of Co^{2+} will lead to the over-dense cross-linking points and restrict the movement of molecular chains. Therefore, the amount of Co^{2+} is critical in determining the generation of cross-linking structure of hydrogels.

To further reveal the mechanical properties of these obtained hydrogels, the rheological properties of these hydrogels were measured. The dynamic rotate strain sweep curves of these prepared hydrogels were taken within the strain ranging from 0.005 % to 350 %. As displayed in Fig. 2c, the dynamic strain sweep curves of these obtained hydrogels have the similar wide linear viscosity region, where storage moduli (G') is higher than loss moduli (G''), illustrating that these hydrogels have the typical gel-like property. Among these prepared hydrogels, the G' value of CGPH-2 is the largest, indicating that the mechanical property of CGPH-2 is the strongest. When the strain increases to 100 %, the G' and the G'' begin to fluctuate and the hydrogel samples appear quasi-liquid states. Compared with the prepared CGPH, the PH and GPH can only stay the gel state ($G' > G''$) within a smaller strain interval, which is mainly due to their poor degree of cross-linking. Notably, the linear decrease of viscosity with angular frequency indicates the presence of chemical cross-linking and physical interaction

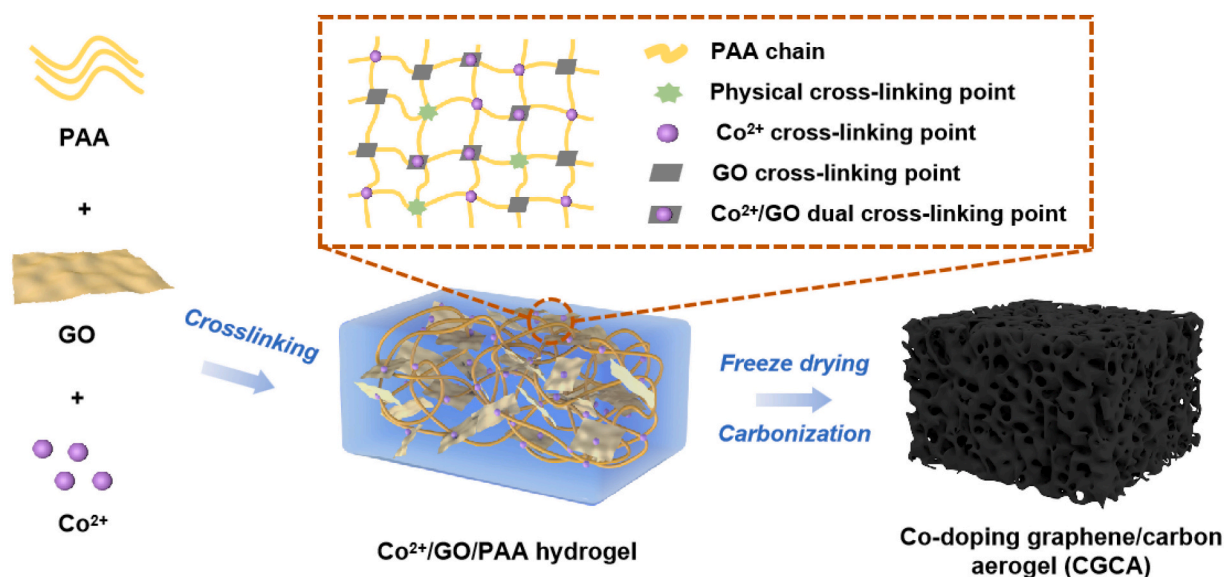


Fig. 1. Schematic of CGCA derived from PAA-based hydrogel.

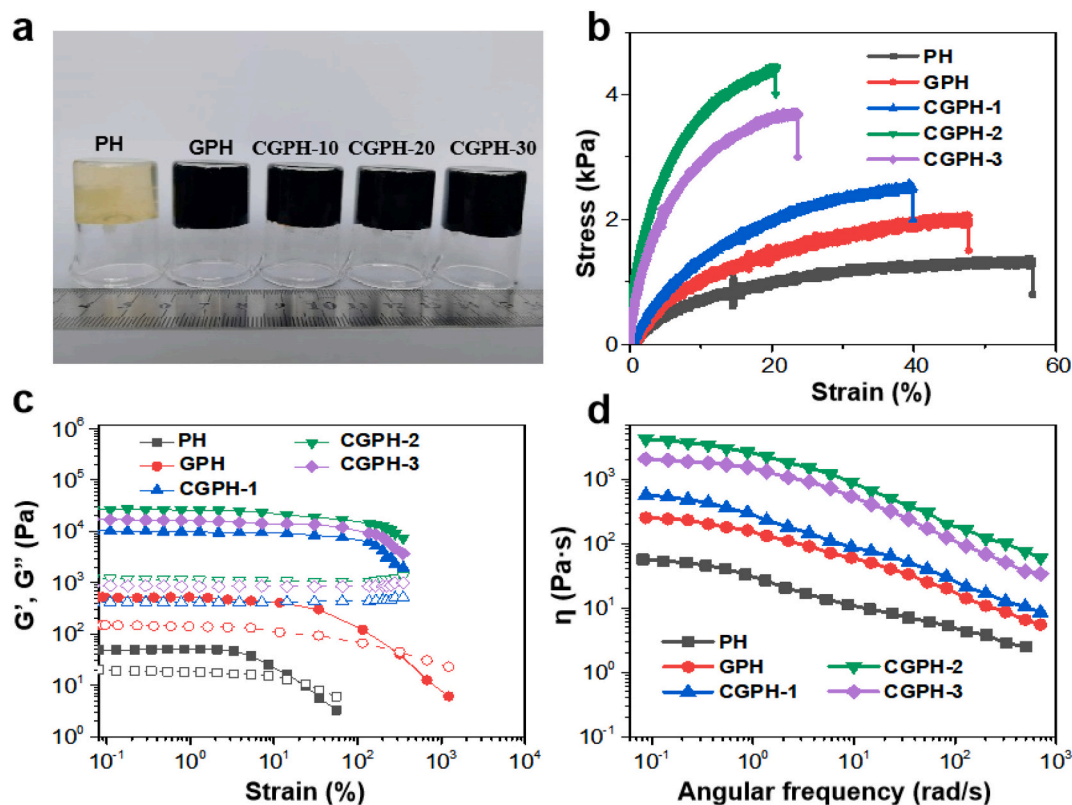


Fig. 2. (a) The gel exhibition and (b) stress-strain curves of different hydrogel samples. (c) Strain sweeps curves at fixed frequency with strain ranging from 0.005 % to 350 % (fixed frequency: 1 Hz). (d) Apparent viscosity of different hydrogel samples with the frequency from 0 to 700 s^{-1} (fixed strain: 0.5 %).

in the sample (Fig. 2d). Significantly, the CGPH-2 has the highest viscosity among these obtained hydrogels, indicating the strongest cross-linking architecture with Co^{2+} and GO dual cross-linking points.

3.2. Morphological and structural characterization

By freeze-drying and carbonization, the porous CA samples were obtained from the prefabricated hydrogels. Primarily, the morphology of these prepared CA samples was observed using the scanning electron

microscopy (SEM). Compared with the PH-derived CA sample (PCA), the pore size of GPH-derived CA sample (GCA) is relatively small (Fig. S1), indicating that the pore size of GCA can be effectively adjusted by using GO cross-linking agent. In the SEM images of these obtained CGCA (Figs. 3a and S2), it can be unambiguously seen that the pore size of these prepared CGCA samples decreases and the density of pores increases with increased amount of Co^{2+} . Obviously, the CGCA-2 exhibits the best porous morphology for the appropriate amount of Co^{2+} . While, the CGCA-3 sample has dense lumpy structure due to the addition of

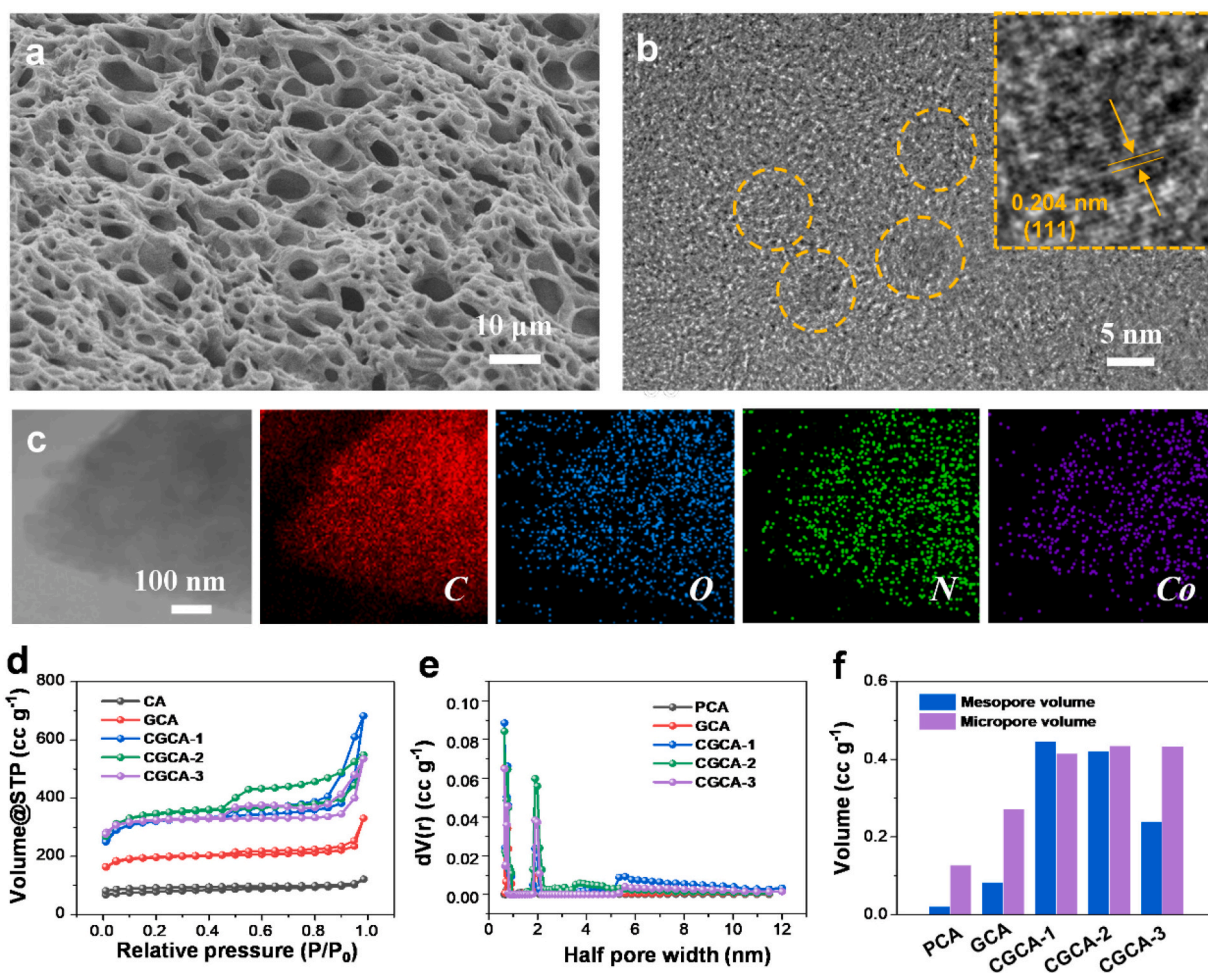


Fig. 3. (a) SEM image, (b) TEM images and (c) corresponding EDS mapping of obtained CGCA-2. (d) N_2 adsorption-desorption isotherms, (e) pore-size distribution and (f) pore volume of the CGCA-2 and control samples.

excessive Co^{2+} . The above results illustrate that the pore structure of CGCA samples can be effectively regulated by controlling the addition of Co^{2+} . To further study the morphology and chemical composition of CGCA-2 sample, transmission electron microscopy (TEM) with X-ray energy dispersive spectroscopy (EDS) mapping was employed. As shown in the TEM image of CGCA-2 (Fig. S3), the hierarchically porous surface can be observed, which is helpful to improve the surface area of the CGCA-2. As shown in the high-resolution TEM image of CGCA-2 (Fig. 3b), the lattice spacing of Co nanoparticle is 0.204 nm, which can be attributed to (111) crystal plane of metallic Co phase. As reported, the doping of Co can effectively promote the conductivity of CA materials [43]. Furthermore, the EDS mapping images of CGCA-2 reveal that the C, N, O and Co elements homogeneously coexist in CGCA-2 sample (Fig. 3c).

Notably, the N_2 adsorption-desorption isotherms of these obtained CA samples are IV-type curves (Fig. 3d), which is due to the presence of mesopores and macropores in these prepared CA samples [44]. Compared with CGCA-1 and CGCA-3, the N_2 adsorption capacity of CGCA-2 increases quickly at relatively low pressures ($P/P_0 < 0.01$) and the hysteresis loop of CGCA-2 is more evident at high pressure ($0.4 \leq P/P_0 < 0.99$), illustrating that the CGCA-2 has more micropores and the pore size of CGCA-2 is smaller than that of CGCA-1 or CGCA-3. By comparing the surface area, pore-size distribution and hole volume of these prepared CA samples (Table S1, Fig. 3e and f), it can be seen that the micropore volume and mesoporous volume of these prepared CGCA samples are much higher than those of GCA and PCA. Especially, the CGCA-2 has the largest micropore volume among these prepared CA

samples, which is beneficial to accelerate ion transport and improve the electrochemical performance.

The X-ray diffraction (XRD) patterns of these obtained CA samples show the broad peaks centered around 24° – 26° (Fig. 4a), which is derived from the (002) crystal plane of graphite. Moreover, in the XRD patterns of CGCA samples, there are three additional XRD peaks at 44.2° , 51.6° and 76.3° , corresponding to the (111), (200) and (220) crystal plane of metallic Co (PDF#15-0806). The graphitization degree of these prepared CA samples was also confirmed by Raman measurements. There are two peaks at 1596 and 1350 cm^{-1} in the Raman spectra of these CA samples (Fig. 4b), which are the peaks of G band and D band [44,45]. The graphitization degree of the CA samples can be evaluated by calculating the ratio of D band and G band. Among these CA samples, the I_D/I_G of CGCA-2 is the lowest, indicating that the graphitization degree of CGCA-2 is the highest. Meanwhile, it is demonstrated that the graphitization degree of the CGCA samples with Co doping is higher than those of PCA and GCA. The results prove that the graphitization degree of CA materials can be greatly improved for the addition of Co^{2+} , so as to improve the conductivity of CA samples.

The chemical states of these prepared CA samples were also investigated with X-ray photoelectron spectroscopy (XPS). Obviously, the XPS spectra of the obtained CGCA samples clearly show the presence of Co elements (Fig. S4). In the high-resolution Co 2p spectra of these obtained CGCA samples (Fig. 4c), the XPS peaks at 797.4 and 781.5 eV correspond to the Co $2p_{1/2}$ and Co $2p_{3/2}$ of Co^{2+} and their two satellite peaks are observed at 786.4 and 803.3 eV [46,47]. Notably, no metallic Co signal peak is detected in the Co 2p spectra of these CGCA sample,

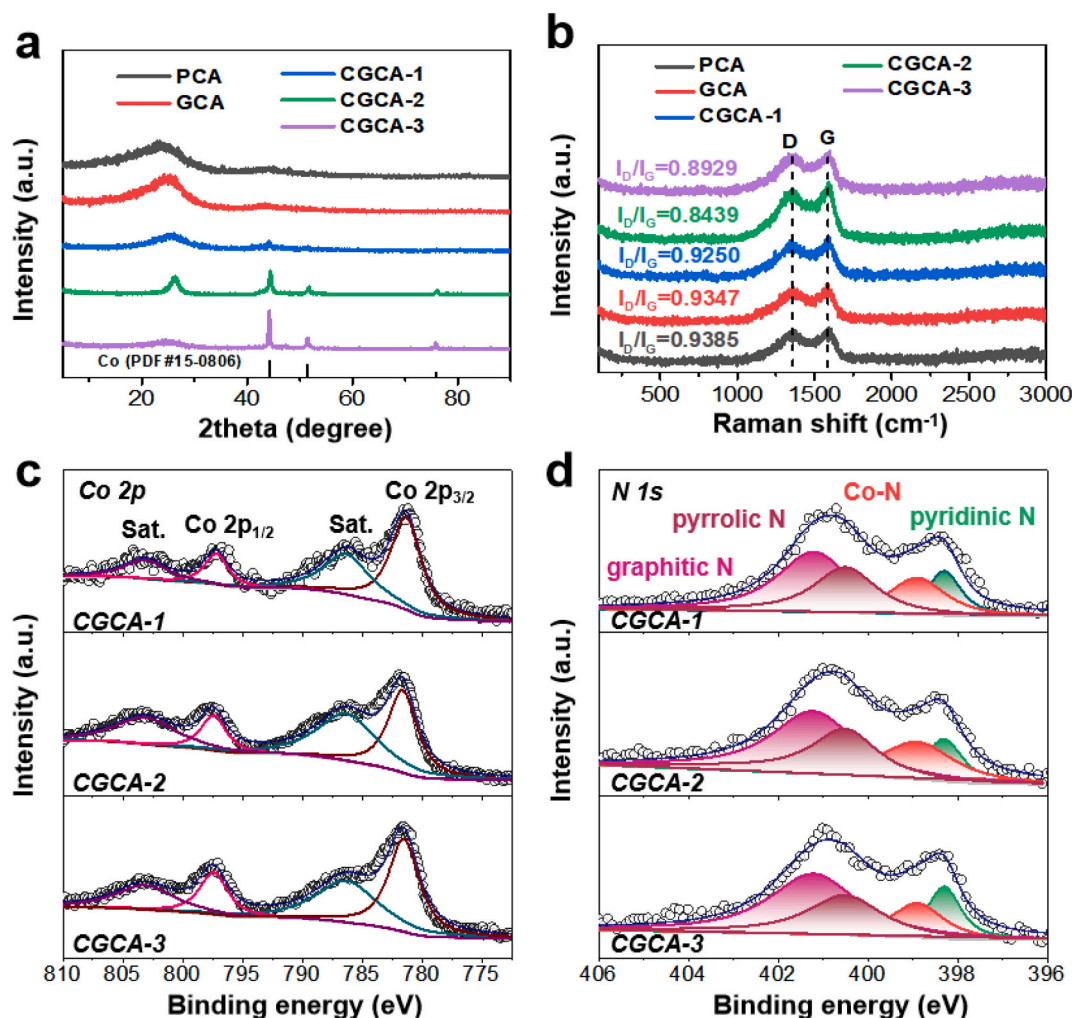


Fig. 4. (a) XRD patterns, (b) Raman spectra, (c) high-resolution Co 2p and (d) high-resolution N 1s spectra of the prepared CGCA samples.

which may be due to the carbon coating on the surface of Co nanoparticles. Meanwhile, the N 1s spectra of these prepared CGCA samples can be resolved into pyridinic N (398.3 eV), Co—N (399.1 eV), pyrrolic N (400.5 eV) and graphitic N (401.2 eV) (Fig. 4d), respectively [48,49]. As report, the presence of Co—N can make contributions to offer high electrical conductivity for the enhanced EDLC-derived capacitive performance [50]. Moreover, the C 1s and O 1s spectra of these obtained CGCA samples indicate that the surfaces of these prepared CGCA samples are rich in oxygen-containing functional groups (Fig. S5). With these nitrogen and oxygen functional groups, these CGCA samples possess good wettability, which makes electrolyte easily permeate into the porous CGCA samples, thus improving their capacitive properties.

3.3. Electrochemical performance

The electrochemical performances of the porous CA samples were tested in a three-electrode system in 1 M H₂SO₄ electrolyte. Obviously, the CV curves feature two distinct redox peaks (Fig. 5a), indicating the predominant EDLC-derived contribution of the carbon component, as well as the pseudo-capacitive contribution of the electrochemically active N species [51–53]. Notably, the CV curve area of CGCA-2 is the largest among these prepared CA samples, representing the highest capacity of CGCA-2. Meanwhile, the galvanostatic charge-discharge (GCD) curves of these prepared CA samples present a set of oxidation-reduction plateaus at around 0.4 and 0.5 V at 1 A g⁻¹ (Fig. 5b), which follows the peak position in the CV curves. Notably, compared with other obtained

CA samples, the CGCA-2 has a much longer GCD curve and shows the excellent electrochemical performance. Moreover, the calculated specific capacities of these CA-based samples at 1 A g⁻¹ demonstrates the largest specific capacity of CGCA-2 (371 F g⁻¹) among these obtained CA samples (Fig. 5c), which outperforms other reported CA-based electrode materials (Table S2). At the same time, the GCD curves of the CGCA-2 were measured at different specific current values from 1 to 150 A g⁻¹ (Fig. S6). The corresponding capacities illustrate that the CGCA-2 has superior rate performance, even maintaining about 57 % at 150 A g⁻¹ (Fig. S7). Meanwhile, the GCD curves of these CA samples were also measured in alkaline electrolyte (Fig. S8), which prove that the CGCA-2 exhibits the best capacitive performance among these CA samples. These results indicate that the CGCA-2 electrode has the best capacitive performance among all the CGCA electrodes, which can be attributed to its large specific surface area and high electrical conductivity.

As shown in the electrochemical impedance spectroscopy (EIS) spectra of CA samples (Fig. S9), the line of CGCA-2 is nearly vertical in the low-frequency region, indicating the internal and charge-transfer resistance of CGCA-2 are relatively low. The above result can be due to the high graphitization degree of CGCA-2. In order to further reveal the intrinsic resistance of these CA samples, the correlation between bode phase angle and frequency was studied. At the frequency of 0.01 Hz, the phase angles of these prepared carbon aerogels are about -90° (Fig. 5d), which illustrates that these obtained CA samples have remarkable capacitive characteristics. The characteristic frequency, that is the frequency corresponding to the phase angle of 45°, is the point at

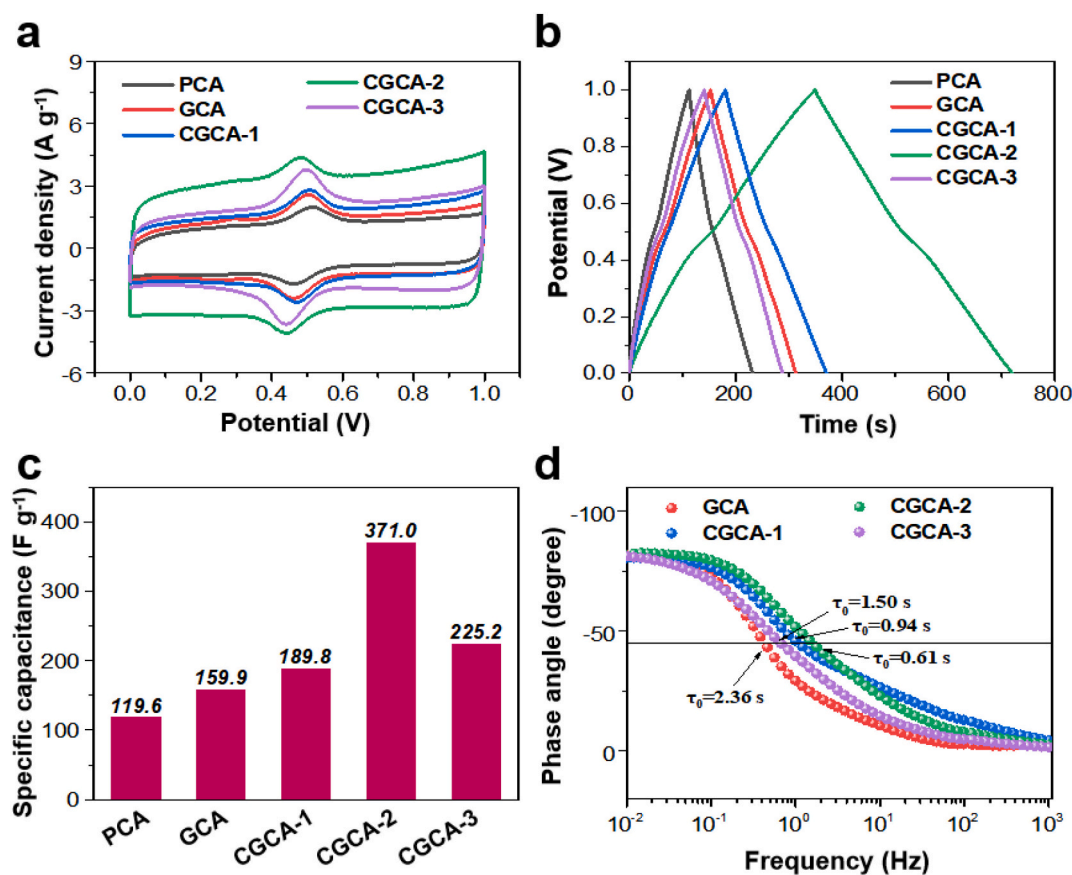


Fig. 5. (a) CV curves at the scan rate of 10 mV s⁻¹, (b) GCD curves at 1 A g⁻¹, (c) specific capacitances and (d) phase angles of the CGCA-2 and control samples.

which the capacitive impedance and resistive impedance are equal [54,55], whose corresponding time constant τ_0 ($1/f_0$) is the shortest time required for the equipment to release all energy. Notably, the τ_0 of GCA, CGCA-1, CGCA-2, CGCA-3 are 2.36, 0.94, 0.61 and 1.50 s, respectively. The result shows that the τ_0 of CGCA-2 is the smallest among these CA samples, which can be due to the highly efficient ion

diffusion within the multiscale pore structure.

As illustrated in Fig. 6a, the symmetric supercapacitors were assembled using CGCA-2 as electrode materials. The Fig. 6b is the CV curves of the supercapacitor device, which are approximately quasi-rectangular at the scan rate from 10 to 200 mV s⁻¹. Meanwhile, the GCD curves present symmetrical triangular in the range of 0.5 to 10 A

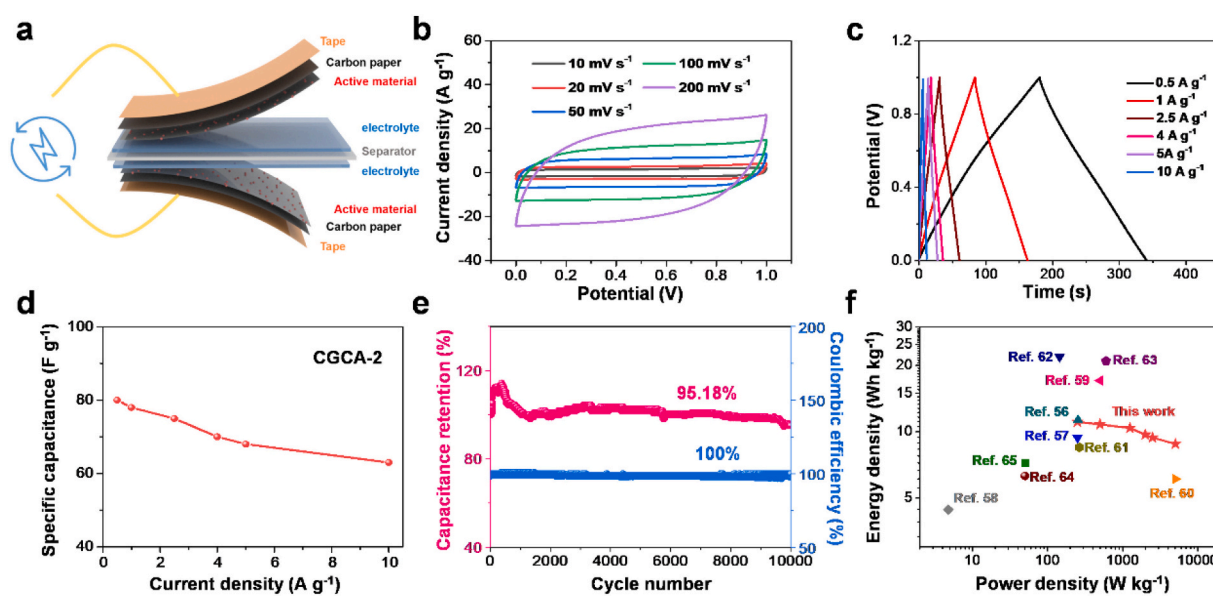


Fig. 6. (a) Schematic of the symmetric supercapacitor. (b) CV curves, (c) GCD curves, (d) specific capacitance, (e) cycling performance and Coulombic efficiency of the symmetric supercapacitor with CGCA-2 electrodes. (f) Ragone plot of the symmetric supercapacitor with CGCA-2 electrodes, in comparison with those reported by other literatures.

g^{-1} (Fig. 6c). Moreover, the specific capacitance of the symmetric supercapacitor is 80 F g^{-1} at 0.5 A g^{-1} and maintains at 63 F g^{-1} at 10 A g^{-1} (Fig. 6d), indicating a perfect capacitance retention of 74 %. After 10,000 cycles, the capacitance retention of the supercapacitor is 95 % and its Coulombic efficiency is nearly 100 % (Fig. 6e), illustrating that the supercapacitor assembled with CGCA-2 electrodes has good cycling stability. As shown in the Fig. S10 and Table S3, we have further carried out the post-mortem XPS measurements of the CGCA-2 sample after the electrochemical tests. It can be found that the content of N element is slightly decreases and the content of Co element appreciably decreases for CGCA-2 after the electrochemical tests, which can be attributed to the corrosion of the N-doped carbon substrate and the dissolution of Co species in the harsh acidic electrolytes and concomitantly the capacitance decay during the electrochemical tests. The EIS measurement was also tested to assess the resistances of the supercapacitor with CGCA-2 electrodes (Fig. S11), which indicates that the device has small diffusion resistance and charge transfer resistance. Furthermore, the Ragone plot of the supercapacitor with CGCA-2 electrodes (Fig. 6f) illustrates that the energy density of the device can reach 11.1 Wh kg^{-1} at a power density of 250 W kg^{-1} , and maintains 8.8 Wh kg^{-1} at a power density of 5029 W kg^{-1} , higher than other reported porous carbon-based electrode materials [56–65]. In addition, the symmetric supercapacitors assembled with CGCA-2 electrodes can also exhibit capacitive energy-storage performance in alkaline electrolyte (Fig. S12). Furthermore, as shown in Fig. S13, the light-emitting diode can be powered by the symmetric supercapacitor with CGCA-2 electrodes.

4. Conclusion

In summary, the Co-doping graphene/carbon hybrid aerogel (CGCA) is prepared via a dual cross-linking strategy and applied for high-performance supercapacitor. Using Co^{2+} and GO sheets as dual cross-linking agents can not only adjust the pore structure of carbon aerogel to increase its capacitive property, but also improve the graphitization of carbon matrix to boost its electrical conductivity. Benefit from these merits, the optimized CGCA electrode shows a typical EDLC behavior with high specific capacitance (371 F g^{-1} at 1 A g^{-1}), superior energy density (11.1 Wh kg^{-1}) and power density (5029 W kg^{-1}), as well as outstanding cycling stability (95 % after 10,000 cycles at 5 A g^{-1}). This work offers insights for further design and advancement of carbon aerogels with modulated hierarchical porosity and enhanced electrical conductivity towards various energy storage devices.

CRediT authorship contribution statement

Guojie Chao: Conceptualization, Investigation, Data curation, Writing – original draft. **Dong Wang:** Investigation, Data curation. **Yang Wang:** Investigation, Data curation. **Xu Zhang:** Data curation, Writing – review & editing. **Suli Chen:** Writing – review & editing. **Yufeng Wang:** Investigation. **Wei Zong:** Investigation. **Wei Fan:** Writing – review & editing. **Longsheng Zhang:** Supervision, Resources, Writing – review & editing. **Tianxi Liu:** Supervision, Resources, Writing – review & editing.

Declaration of competing interest

The authors declare that they have no known competing financial interests or personal relationships that could have appeared to influence the work reported in this paper.

Data availability

Data will be made available on request.

Acknowledgements

This work was financially supported by the National Natural Science

Foundation of China (52103260, 52161135302), Natural Science Foundation of Jiangsu Province (BK20210482), China Postdoctoral Science Foundation (2021M690067), Jiangsu Province Postdoctoral Science Foundation (2021K053A) and Fundamental Research Funds for the Central Universities (2232019A3-03).

Appendix A. Supplementary data

Supplementary data to this article can be found online at <https://doi.org/10.1016/j.est.2022.105445>.

References

- [1] Z. Zhao, K. Xia, Y. Hou, Q. Zhang, Z. Ye, J. Lu, *Chem. Soc. Rev.* 50 (2021) 12702–12743.
- [2] E. Dhandapani, S. Thangarasu, S. Ramesh, K. Ramesh, R. Vasudevan, N. Duraisamy, *J. Energy Storage* 52 (2022), 104937.
- [3] W. Zong, H. Guo, Y. Ouyang, L. Mo, C. Zhou, G. Chao, J. Hofkens, Y. Xu, W. Wang, Y. Miao, G. He, I.P. Parkin, F. Lai, T. Liu, *Adv. Funct. Mater.* 32 (2022), 2110016.
- [4] M. Hu, H. Zhang, T. Hu, B. Fan, X. Wang, Z. Li, *Chem. Soc. Rev.* 49 (2020) 6666–6693.
- [5] L. Li, Y. Zhang, H. Lu, Y. Wang, J. Xu, J. Zhu, C. Zhang, T. Liu, *Nat. Commun.* 11 (2020) 62.
- [6] Y. Chen, T. Zhou, L. Li, W.K. Pang, X. He, Y. Liu, Z. Guo, *ACS Nano* 13 (2019) 9376–9385.
- [7] S. Ghosh, S. Barg, S.M. Jeong, K. Ostrikov, *Adv. Energy Mater.* 10 (2020), 2001239.
- [8] L. Zhang, W. Fan, W. Tjiu, T. Liu, *RSC Adv.* 5 (2015) 34777–34787.
- [9] P. Xie, W. Yuan, X. Liu, Y. Peng, Y. Yin, Y. Li, Z. Wu, *Energy Storage Mater.* 36 (2021) 56–76.
- [10] H. Peng, B. Yao, X. Wei, T. Liu, T. Kou, P. Xiao, Y. Zhang, Y. Li, *Adv. Energy Mater.* 9 (2019), 1803665.
- [11] M. Salanne, B. Rotenberg, K. Naoi, K. Kaneko, P.L. Taberna, C.P. Grey, B. Dunn, P. Simon, *Nat. Energy* 1 (2016) 16070.
- [12] K. Wu, Q. Liu, *Appl. Surf. Sci.* 379 (2016) 132–139.
- [13] F. Mo, H. Zhang, Y. Wang, C. Chen, X. Wu, *J. Energy Storage* 49 (2022), 104122.
- [14] K. Subhani, X. Jin, P.J. Mahon, A.K.T. Lau, N.V. Salim, *Compos. Commun.* 24 (2021), 100663.
- [15] C. Zhao, Y. Wang, J. Zheng, S. Xu, P. Rui, C. Zhao, *J. Power Sources* 521 (2022), 230942.
- [16] V. Rodriguez-Mata, J. Hernandez-Ferrer, C. Carrera, A.M. Benito, W.K. Maser, E. Garcia-Bordej, *Energy Storage Mater.* 25 (2020) 740–749.
- [17] K. Wei, F. Zhang, Y. Yang, B. Zhai, X. Wang, Y. Song, *J. Energy Storage* 51 (2022), 104342.
- [18] G. Lv, X. Dai, Y. Qiao, Q. Tan, Y. Liu, Y. Chen, *Chem. Eng. J.* 448 (2022), 137660.
- [19] S. Barg, F.M. Perez, N. Ni, P.D.V. Pereira, R.C. Maher, E. Garcia-Tunn, S. Eslava, S. Agnoli, C. Mattevi, E. Saiz, *Nat. Commun.* 5 (2014) 4328.
- [20] C.H.J. Kim, D. Zhao, G. Lee, J. Liu, *Adv. Funct. Mater.* 26 (2016) 4976–4983.
- [21] L. Zuo, Y. Zhang, L. Zhang, Y. Miao, W. Fan, T. Liu, *Materials* 8 (2015) 6806–6848.
- [22] R. Chen, X. Li, Q. Huang, H. Ling, Y. Yang, X. Wang, *Chem. Eng. J.* 412 (2021), 128755.
- [23] S. Long, Y. Feng, F. He, J. Zhao, T. Bai, H. Lin, W. Cai, C. Mao, Y. Chen, L. Gan, J. Liu, M. Ye, X. Zeng, M. Long, *Nano Energy* 85 (2021), 105973.
- [24] J. Shao, J. Xiao, Y. Wang, H. Zhou, A. Yuan, *ChemistrySelect* 5 (2020) 5323–5329.
- [25] M. He, M.K. Alam, H. Liu, M. Zheng, J. Zhao, L. Wang, L. Liu, X. Qin, J. Yu, *Compos. Commun.* 28 (2021), 100936.
- [26] Z. Chen, S. Zhao, H. Zhao, Y. Zou, C. Yu, W. Zhong, *Chem. Eng. J.* 409 (2021), 127891.
- [27] L. Li, J. Meng, M. Zhang, T. Liu, C. Zhang, *Chem. Commun.* 58 (2022) 185–207.
- [28] J. Shao, J. Feng, H. Zhou, A. Yuan, *Appl. Surf. Sci.* 471 (2019) 745–752.
- [29] P. Lv, X. Tang, R. Zheng, X. Ma, K. Yu, W. Wei, *Nanoscale Res. Lett.* 12 (2017) 630.
- [30] S. Yuan, W. Fan, D. Wang, L. Zhang, Y. Miao, F. Lai, T. Liu, *J. Mater. Chem. A* 9 (2021) 423–432.
- [31] H. Huang, L. Xia, Y. Zhao, H. Zhang, T. Cong, J. Wang, N. Wen, S. Yang, Z. Fan, L. Pan, *Electrochim. Acta* 364 (2020), 137297.
- [32] Y. Chen, G. Dai, Q. Gao, *ACS Sustain. Chem. Eng.* 7 (2019) 14064–14073.
- [33] Y. Zhang, W. Fan, Y. Huang, C. Zhang, T. Liu, *RSC Adv.* 5 (2015) 1301–1308.
- [34] R. Zhao, H. Peng, H. Wang, J. Liang, Y. Lv, G. Ma, Z. Lei, *J. Energy Storage* 28 (2020), 101174.
- [35] D. Fan, X. Yang, J. Liu, P. Zhou, X. Zhang, *Compos. Commun.* 27 (2021), 100887.
- [36] B. Li, Y. Cheng, L. Dong, Y. Wang, J. Chen, C. Huang, D. Wei, Y. Feng, D. Jia, Y. Zhou, *Carbon* 122 (2017) 592–603.
- [37] P. Gao, J. Lei, J. Tan, G. Wang, H. Liu, L. Zhou, *Compos. Commun.* 25 (2021), 100736.
- [38] W. Zong, N. Chui, Z. Tian, Y. Li, C. Yang, D. Rao, W. Wang, J. Huang, J. Wang, F. Lai, T. Liu, *Adv. Sci.* 8 (2021), 2004142.
- [39] D. Li, D. Yang, X. Yang, Y. Wang, Z. Guo, Y. Xia, S. Sun, S. Guo, *Angew. Chem. Int. Ed.* 55 (2016) 15925–15928.
- [40] Y. Wang, M. Tebyetekerwa, Y. Liu, M. Wang, J. Zhu, J. Xu, C. Zhang, T. Liu, *Chem. Eng. J.* 420 (2021), 127637.
- [41] F. Yang, X. Zhao, T. Xue, S. Yuan, Y. Huang, W. Fan, T. Liu, *Sci. China Mater.* 64 (2021) 1267–1277.

- [42] Y. Yang, W. Fan, S. Yuan, J. Tian, G. Chao, T. Liu, J. Mater. Chem. A 9 (2021) 23968–23976.
- [43] Y. Song, M. Zhang, T. Liu, T. Li, D. Guo, X. Liu, Nanomaterials 9 (2019) 1110.
- [44] K. Zhang, F. Xiong, J. Zhou, L. Mai, L. Zhang, Nano Energy 67 (2020), 104222.
- [45] G. Chao, L. Zhang, J. Tian, W. Fan, T. Liu, Compos. Commun. 25 (2021), 100703.
- [46] W. Yang, X. Shi, Y. Li, P. Huan, J. Energy Storage 26 (2019), 101018.
- [47] Q. Ma, G. Du, B. Guo, W. Tang, Y. Li, M. Xu, C. Li, Chem. Eng. J. 388 (2020), 124210.
- [48] T. Zhu, S. Liu, K. Wan, C. Zhang, Y. Feng, W. Feng, T. Liu, ACS Appl. Energy Mater. 3 (2020) 4949–4957.
- [49] G. Chao, L. Zhang, D. Wang, S. Chen, H. Guo, K. Xu, W. Fan, T. Liu, Carbon 159 (2020) 611–616.
- [50] P.A. Shinde, N.R. Chodankar, M.A. Abdelkareem, Y.K. Han, A.G. Olabi, Chem. Eng. J. 428 (2022), 131888.
- [51] L. Huang, Z. Luo, M. Luo, Q. Zhang, H. Zhu, K. Shi, S. Zhu, J. Energy Storage 38 (2021), 102509.
- [52] C. Fan, Y. Tian, S. Bai, C. Zhang, X. Wu, J. Energy Storage 44 (2021), 103492.
- [53] L. Yao, D. Chen, S. Yan, J. Lin, Y. Liu, J. Lian, Y. Liu, H. Lin, S. Han, ChemistrySelect 4 (2019) 2726–2733.
- [54] C. Xiong, M. Li, W. Zhao, C. Duan, Y. Ni, J. Materiomics 6 (2020) 523–531.
- [55] N. Islam, J. Warzywoda, Z.Y. Fan, Nano-Micro Lett. 10 (2018) 9.
- [56] C. Jiang, Z. Wang, J. Li, Z. Sun, Y. Zhang, L. Li, K.-S. Moon, C. Wong, Electrochim. Acta 353 (2020), 136482.
- [57] S. Lv, L. Ma, X. Shen, H. Tong, J. Electroanal. Chem. 907 (2022), 116060.
- [58] L. E, W. Gan, J. Sun, Z. Wu, C. Ma, W. Li, S. Liu, Energy Fuels 35 (2021) 8295–8302.
- [59] Y. Ping, S. Yang, J. Han, X. Li, H. Zhang, B. Xiong, P. Fang, C. He, Electrochim. Acta 380 (2021), 138237.
- [60] M. Xu, A. Wang, Y. Xiang, J. Niu, J. Clean. Prod. 315 (2021), 128110.
- [61] W. Han, L. Yuan, X. Liu, C. Wang, J. Li, J. Electroanal. Chem. 899 (2021), 115643.
- [62] L. E, J. Sun, W. Gan, Z. Wu, Z. Xu, L. Xu, C. Ma, W. Li, S. Liu, J. Energy Storage 38 (2021) 102414.
- [63] R. Zhong, H. Zhang, Y. Zhang, P. Yue, X. Wu, J. Energy Storage 51 (2022), 104346.
- [64] B. Thomas, G. George, A. Landstrom, I. Concina, S. Geng, A. Vomiero, M. Sain, K. Oksman, ACS Appl. Electron. Mater. 3 (2021) 4699–4710.
- [65] L. Wang, Q. Wu, B. Zhao, Z. Li, Y. Zhang, L. Huang, S. Yu, J. Colloid Interface Sci. 605 (2022) 790–802.